Precision Engineering 92 (2025) 207–218

Contents lists available at ScienceDirect

Precision Engineering

journal homepage: www.elsevier.com/locate/precision

Surface topography analysis in cold spray additive manufacturing

Paloma Sirvent [a,*], Ana Lozano [a], Miguel A. Garrido-Maneiro [a], Pedro Poza [a,b], Rordolpho F. Vaz [c,d], Vicente Albaladejo-Fuentes [c], Irene G. Cano [c]

[a] DIMME – Durability and Mechanical Integrity of Structural Materials, Escuela Superior de Ciencias Experimentales y Tecnología, Universidad Rey Juan Carlos, C/ Tulipán s/n, 28933, Móstoles, Madrid, Spain
[b] Instituto de Tecnologías para la Sostenibilidad. Universidad Rey Juan Carlos, Spain
[c] Thermal Spray Centre (CPT), Department of Materials Science and Physical Chemistry, Universitat de Barcelona. C/ Martí i Franquès, 1, 7th Floor, 08028, Barcelona (Barcelona), Spain
[d] Center for Thermal Spray Research (CTSR). Stony Brook University, Room 130 Heavy Engineering Bldg, 11790, Stony Brook, NY, United States

ARTICLE INFO

Handling Editor: Dr. S Ludwick

Keywords:
Cold spray additive manufacturing
Aluminum
Titanium
Topography
Microstructure
Nanoindentation

ABSTRACT

Additive manufacturing, and particularly the cold spray technology for additive manufacturing (CSAM), is fast becoming a key technology to produce components in an efficient and environmentally friendly manner. This method usually requires a final rectification to generate specific surface topographies. The novelty of this paper is related to the capabilities of the CSAM technique to control the surface topography of the samples. Thus, this work investigates the topography of CSAM samples and its correlation with the processing parameters. Pure Al and Ti samples were manufactured following two different deposition strategies: traditional and metal knitting. This last strategy constitutes a promising alternative for CSAM to obtain near-net-final shape components. The topography was analyzed by confocal microscopy considering the form, waviness, and roughness components. Moreover, the microstructure and mechanical properties of the samples were also investigated in order to assure reliable freestanding CSAM deposits. Results showed that the waviness was controlled by the spraying line spacing, and that the waviness and roughness profiles of the metal knitting samples presented the largest wavelengths regardless the material. The metal knitting method generated samples with higher thickness and porosity than the traditional strategy, while the mechanical properties at the local scale were not varied. The study highlights the CSAM technology potential for controlling the deposit's surface topography.

1. Introduction

Additive Manufacturing (AM) has been proposed as an alternative to the traditional processes for producing components with defined geometry. AM creates near-net-shape parts, and the final piece is commonly obtained after a finishing machining stage. This process significantly reduces the amount of waste generated, making it an environmentally friendly alternative [1].

Recently, the cold spray technique (CS) has been revealed as a promising candidate for additive manufacturing (CSAM) due to its low deposition temperature [2,3]. During the CSAM process, fine powder particles are accelerated in a high velocity compressed gas stream at temperatures below their melting point. The particles impact onto a target plate, deforming and bonding together to produce a layer. A CSAM deposit is built up layer-by-layer to form a part or component. Therefore, the kinetic energy of the particles is turned into high strain and heat. Consequently, the CS manufacturing process is dominated by the plastic deformation of the spraying particles. Then, the processing characteristics by CS do not significantly change the properties of the feedstock powder by heating or melting during the CSAM part fabrication, and also prevents the materials oxidation during the deposition [4,5].

One of the challenges in CSAM fabrication is to improve the geometrical precision of the sprayed samples to obtain near-net shape components. Particularly, the nozzle path during the deposition process can significantly improve the geometric quality of the component. The traditional strategy is based on a linear zigzag-like and normal movement of the nozzle regarding the target surface, which might be reproduced to spray the consecutive layers, or it might be done by alternating the spraying directions. This sequence promotes the sidewalls growth out of the normal angle with the target surface. Furthermore, the greater the thickness of the deposited material, the more relevant this geometric

* Corresponding author.
E-mail address: paloma.sirvent@urjc.es (P. Sirvent).

https://doi.org/10.1016/j.precisioneng.2024.12.007
Received 30 July 2024; Received in revised form 27 November 2024; Accepted 6 December 2024
Available online 9 December 2024
0141-6359/© 2024 The Authors. Published by Elsevier Inc. This is an open access article under the CC BY-NC-ND license (http://creativecommons.org/licenses/by-nc-nd/4.0/).

deviation is, resulting in a pyramid-like shape. However, it is possible to compensate this undesirable geometry by imposing an optimal sequence of movements to the CS nozzle. Recently, some researchers have developed methods to obtain near-net-final shape CSAM parts by imposing optimal nozzle trajectories using a robot arm system [6,7]. One of these strategies is known as metal knitting (MK). MK consists of spraying with a circular movement at an angle different from the normal one [6].

Previous studies have demonstrated the MK strategy effectiveness in generating components by CSAM with a dimensional tolerance close to the final one for metallic alloys [6,8]. Vaz et al. [6] generated CSAM parts of 316L stainless steel, pure Cu, pure Al, pure Ti, and Ti6Al4V using MK and traditional strategies. They evaluated the obtained geometry by inspecting the sidewall angles, and visual characteristics of the parts. They observed that MK strategy makes feasible controlling the sidewall angles during the build-up, which is not possible by employing the traditional strategy.

Furthermore, the differentiating characteristics of the MK process may also include the generation of a distinctive controlled surface topography, what has been little explored until the date. The surface topography plays an important role in the performance of the components. It has a decisive influence on friction and wear under lubrication or dry friction conditions [9], as well as on the surface adhesion conditions of substances and bacteria [10,11], and on its wettability [12]. Friction and wear can be increased or decreased by changing the surface topography in lubricated or dry tribological systems [13]. Grutzmacher et al. [10] reported that the surface irregularities have the functions of storing debris and lubricants, reducing the actual contact area, and helping to decrease the damage by wear. Regarding wear in dry sliding conditions, Wang et al. [14] found a correlation between the surface topography parameters and wear resistance for a hardened mold steel. They concluded that the parameter with the strongest effect on wear was the sharpness of the surface height distribution, and the weakest was the largest height. Additionally, the values of these surface topography parameters may change during the wear processes in a surface topography transition phenomenon. This transition can affect the functional performance of machined components, such as friction, lubrication, wear, and contact mechanics [15]. Most of the surface topography changes occur in the first few sliding wear cycles and are caused by asperity removal. Surface profilometry measurements reported by Sakhamuri et al. [16] showed that the reduction in roughness during sliding tests was due to wear and plastic deformation. Both phenomena decreased the height of the peaks. Consequently, the topography of the surfaces in contact depends on the material's properties in contact and the wear mechanisms. This effect is more pronounced in abrasive wear, where a hard material wears a softer material. Generally, as the surface roughness of the hard material increases, the wear intensifies, with a consequent increase in wear rates [17]. Conversely, in dry contacts between ductile materials of similar hardness, the roughness is modified from the first steps of the relative sliding process between the surfaces in contact. The plastic deformation suffered by the asperities, and subsequent formation of mechanically mixed layers, significantly control the evolution of the wear process [18]. In lubricated tests, the contact between surfaces is limited, reducing the effect of surface topography on the wear process [19].

Additionally, surface topography plays a crucial role in the adhesion of bacteria, and thus, surface irregularities are designed to control it. Specifically, the size ratio of bacteria and topography wavelengths seem to be the parameters that determine the adhesion process of bacteria on surfaces [11]. Consequently, there is the possibility of controlling the behavior of materials at a surface level through features generated by specific or random surface topography profiles. Regarding the wettability, various studies have reported that its behavior can transit from hydrophilic to hydrophobic by increasing the size of pores from tens to hundreds of nanometers [12,20]. Therefore, there is a clear dependence between the surface properties and its topography.

The surface topography of CSAM samples has been generally measured by contact profilometry [21] or confocal microscopy [22]. The roughness data is usually reported by means of the ISO roughness parameters, such as average roughness (R_a), root mean square roughness (R_q), and roughness depths (R_z). These are the most important parameters to evaluate the vertical characteristics of the surface deviations [23]. However, these parameters do not give a complete information about the topography of the surface. To carry out a complete characterization of the surface topography, the surface profile should be segregated into three contributions that, ordered from largest to smallest scale, are: form, waviness, and roughness. A topographic characterization at these different scales is of special interest when the contact between surfaces is examined and the behavior of materials in contact intends to be predicted. The quantification of the surface topography allows to predict the contact area and, consequently, the pressure concentration factors. Different works have investigated the waviness and roughness surface profiles to study their influence on the contact pressure distribution [24], to simulate the hydrodynamic pressure evolution under lubrication regime [25], or to determine the influence of the surface topography on the abrasive wear [26]. Consequently, the topographic characterization at different scales may help to optimize surfaces to achieve better tribological performances.

The study of the surface topography generated on CS samples has been generally focused on minimizing the surface irregularities [22,27,28]. Research in this field has shown that the roughness of the sprayed samples is dependent on the particles impact velocity [22] and on the step between spraying lines [27]. The published results related to the surface topography are the ISO roughness parameters, but only few studies provide a detailed description of the surface irregularities based on the profile generated by different wavelength contributions [29]. Besides that, the modification of the surface topography of CSAM samples has been typically achieved by post-processing the sprayed CSAM samples using different techniques: chemical material removal, laser micro-machining, mechanical machining or mechanical treatments [30].

The aim of this work is to analyze the capacity of CSAM to generate specific surface topographies to improve the manufactured components performance. For this purpose, this research has analyzed the correlation between the surface topography of CSAM samples with the processing parameters. The evaluated samples were Al and Ti CSAM components manufactured by two deposition strategies: traditional and MK. Pure Al and Ti materials were selected for this study because these lightweight materials and their alloys have found a market space in the last decades, due to the increasing demand to reduce emissions and improve the fuel economy in the automotive and aerospace industries [31,32]. A topography measurement procedure is proposed to discriminate the effect of the different manufacturing factors on the topography profile components: form, waviness, and roughness. Additionally, the microstructure's morphology and phase analysis were carried out using optical and electron microscopy. Also, the mechanical properties of the samples have been evaluated using the instrumented indentation technique. Therefore, a comparative study of the microstructure and mechanical properties between samples manufactured by traditional and MK deposition sequence has also been included.

2. Materials and experimental methods

2.1. Materials

The materials evaluated in this work were pure Al and pure Ti manufactured by means of the high-pressure CS technique, using a Plasma Giken PCS100 equipment. The samples were sprayed on 100 × 100 × 3 mm^3 1008 steel plate substrates, previously grit-blasted to clean their surfaces and reach a roughness $R_a > 6$ μm, which were detached from the CSAM samples after spraying. The Al and Ti powders were fabricated by water-atomization.

Two types of sample's manufacturing strategies were studied for each material: traditional (T) and metal knitting (MK). The CS parameters are presented in Table 1 and the spraying strategies parameters are presented in Table 2. Fig. 1 shows a schematic representation of the spraying sequence of both strategies, T and MK, based on the scheme of deposition showed by Vaz et al. [6]. The T strategy was performed at an angle of 90° regarding the substrate plane, and the gun movement was linear and bidirectional with a step between layers of 1 mm. Conversely, the MK samples were sprayed at an angle of 60° regarding the substrate plane, and the gun motion was a combination of a rotational movement and a lineal movement, which was bidirectional and with a step of 2 mm.

2.2. Surface topography measurements

The surface topography was directly measured over the as-manufactured samples' surfaces. The surface profiles were performed by confocal microscopy using an RTEC Instrument Universal Profilometer UP-24.

Six 3D images were obtained along each sample, separating the images a minimum of 3 cm from the others and from the edges, with an optical resolution of 0.94 μm and a vertical resolution of 72 nm. Then, a minimum of three linear profiles were acquired from each image, following the perpendicular direction to the spraying lines. The analysis of the linear profiles was carried out through the open-source code Gwyddion. Fig. 2 presents an example of a 3D image obtained by confocal microscopy, the transversal profile selection, and its corresponding topography profile for a Ti-MK sample.

The surface topography analysis has been done by discriminating between the roughness, waviness and form profiles that constitute the surface profile. This means that the topography profile is divided into three profiles considering different wavelength ranges. The largest wavelengths correspond to the form, the lowest ones to the roughness, and the ones in between conform the waviness. The wavelength at which each profile is divided, are known as the cut-off wavelengths (λ). In the present study, the cut-off wavelengths, as well as the evaluation length for the topography analysis (l_e), were selected by following the ISO 4287 [33], ISO 4288 [34], and ISO 11562 standards [35]. In this procedure, the WSm and RSm parameters are used, which measure the mean width of the waviness and roughness profile elements within the evaluation length, respectively. Both parameters are defined by Equation (1), where S_i is the width of the irregularity i. The WSm and RSm values that have been considered for each sample are reported in Table 3, along with their respective λ and the frequency ranges, ν, according to the standards. The table does not differentiate between Al or Ti samples because the necessary λ were similar for both materials.

$$WSm, RSm = \frac{1}{n}\sum_{i=1}^{n} S_i \qquad \text{Equation 1}$$

Then, the waviness and roughness profiles were used to calculate the arithmetical mean height (W_a, R_a), the maximum height of profile (W_z, R_z) and the root mean square deviation (W_q, R_q) parameters (ISO 21920 [36]). The W_a and R_a parameters measure the average deviation of the heights (z(x)) of the waviness and roughness irregularities from the mean line along the sampling length (l_e), respectively, as described by Equation (2). Therefore, it represents the average height of the profile. The W_q and R_q are the root mean square of the waviness and roughness, respectively, defined by Equation (3). Finally, the W_z and R_z are the average of the addition of the five highest peaks (Z_p) and the five lowest valleys (Z_v) of the waviness and roughness profiles along the evaluation length (Equation (4)), respectively. The evaluation length is divided into five sections lengths (l_{sc}) and the highest peak and lowest valley of each section are selected.

Table 1
CS parameters.

Material	Gas	Gas Pressure (MPa)	Gas Temperature (°C)
Al	N_2	3.0	450
Ti	N_2	6.0	900

Table 2
Spraying strategy parameters.

Strategy	Standoff distance (mm)	Angle with the substrate plane (°)	Radius (mm)	Step (mm)
Traditional	40	90	N/A	1.0
Metal Knitting	30	60	2.0	2.0

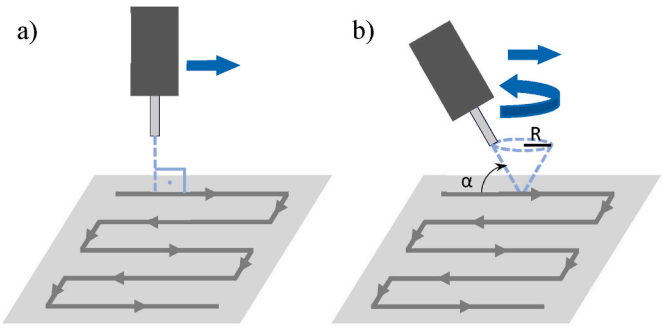

Fig. 1. Schematic representation of the spray gun movement during the CSAM process conducted by means of the a) traditional and b) metal knitting strategies.

$$W_a, R_a = \frac{1}{l_e}\int_0^{l_e} |z(x)|dx \qquad \text{Equation 2}$$

$$W_q, R_q = \sqrt{\frac{1}{l_e}\int_0^{l_e} z^2(x)dx} \qquad \text{Equation 3}$$

$$W_z, R_z = \frac{1}{5}\sum_{i=1}^{5} Zp_i + Zv_i \qquad \text{Equation 4}$$

2.3. Morphological and microstructural characterization

The particles shape, samples morphology and microstructural composition were analyzed by scanning electron microscopy (SEM) in a Hitachi S-3400 equipment, with a Brucker detector for energy dispersive X-ray microanalysis (EDX). Secondary and backscatter electron images (SEI and BSEI respectively), with compositional contrast, were used. Moreover, the particle size distribution of the feedstock powders was characterized by dry mode laser scattering (LS) technique using a Beckman Coulter LS13320 equipment, according to the ASTM B822-02 standard. For the LS dry mode, it is assembled to the equipment the Tornado DPS system device, where the powder is sucked without a suspension medium, e.g. water or ethanol, and flows through the laser illumination/detector system.

An optical microscope (OM) Zeiss Axioscope 5 and its image analysis software were used to obtain the samples thickness and porosity. The porosity and thickness measurements were done on panoramic images of the samples cross-sections. Ten images were used to calculate the average and standard deviation of both parameters. The porosity values obtained from each image corresponded to the area fraction of pores within the evaluated area. Besides that, a microstructural study was done by SEM, and a qualitative chemical composition evaluation was done by EDX. To conduct the microstructural study, the samples were metallographically prepared on their transversal and parallel cross-sections to the spraying direction, following the ASTM E1920 and

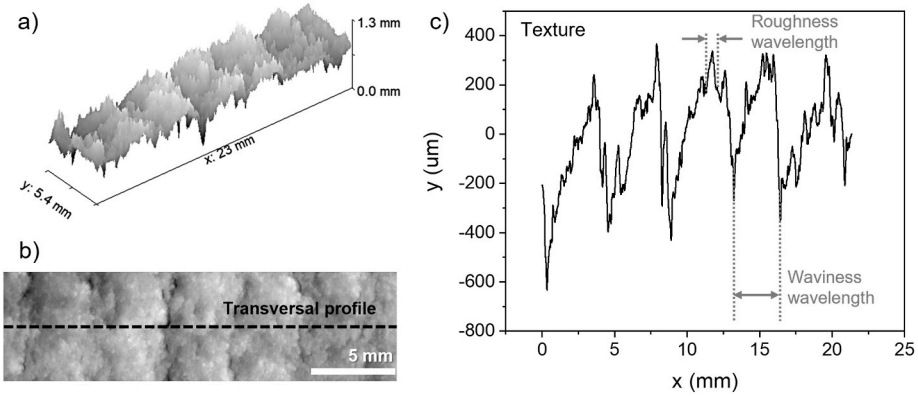

Fig. 2. a) 3D image obtained by confocal microscopy, b) its corresponding 2D image indicating the transversal profile selection, and c) the graphical representation of the topography transversal profile.

Table 3
RSm and cut-offs with the corresponding frequency ranges used to separate the topography profiles of the T and MK samples.

CS sample	Profile	WSm, RSm (mm)	Cut-off, λ (ISO 4288)	Frequency range (1/mm)
Traditional	**Waviness**	2	8	$0.125 < \nu < 1.25$
	Roughness	<0.4	0.8	$\nu > 1.25$
Metal Knitting	**Waviness**	4	8	$0.125 < \nu < 0.4$
	Roughness	<1	2.5	$\nu > 0.4$

ASTM E3 standards. The samples were mounted in a low-stiffness resin after cutting with an alumina cutting wheel for the Al samples, and with a diamond cutting wheel for the Ti samples. All the samples were smoothed and polished in a typical multistep process for these materials until reaching a mirror finish. The final step was done using a suspension of alumina of 0.05 μm.

2.4. Mechanical properties characterization

Nanoindentation tests were performed to evaluate the mechanical properties of the material itself, without the effect of microscopic defects, such as porosity. A nanoindenter Agilent G200 was used with a Berkovich indenter to measure the asymptotic hardness (H_0) and elastic modulus (E) on the samples cross-sections. The samples were prepared following the same polishing procedure employed for the microstructural characterization. The H_0 and E were evaluated as a function of the penetration depth at a total of three heights along the samples' thicknesses to analyze any possible variations. These properties were evaluated on the samples' cross-sections at percentage distances from the substrate regarding the total sample thickness of 25 %, 50 % and 75 %. For this purpose, the samples' thicknesses were measured first, and then the 25 %, 50 % and 75 % values of the sample thickness were determined. Arrays of 30 indents were conducted at each one of the three positions, and it was left a separation between indents of 50 μm to avoid interactions between measurements. The tests were conducted using the continuous stiffness measurement technique (CSM), where multiple loading-unloading cycles were superimposed to a main loading process. The multiple cycles were performed at a frequency of 35 Hz with an amplitude of 2 nm, and the maximum penetration depth of the main loading was established at 2000 nm. Therefore, the hardness (H) and E data could be calculated as a function of penetration depth using the Oliver and Pharr method [37]. There was some effect on the nanoindentation tests due to the presence of pores in the sample. This effect was avoided by selecting the data range available for the measurements, which was determined as the data presenting a linear trend between the indentation depth and the harmonic contact stiffness. The H_0 value was estimated by means of the proportional specimen resistance model (PSR) [38] when the indentation size effect was present along the evaluation data range [39]. The indenter was calibrated to obtain the recording of the actual contact area as a function of the actual contact depth to calculate the mechanical properties [40]. Two calibrations were obtained, one on a bulk of pure Al and another one on a bulk of a Ti6Al4V alloy, which were used for the measurements performed on the Al and Ti samples, respectively.

3. Results

3.1. Feedstock powder characterization

The feedstock powders used to manufacture the samples were pure Al and Ti, which showed an irregular shape, as seen in Fig. 3a and b. This irregular shape is typical of the water-atomized powders. Furthermore, it was observed in the SEM images (Fig. 3a and b) that the Ti particles had a morphology in which edges were predominant, while the Al particles presented a more rounded external profile. The BSE images of the powder, which consist of element contrasted images, have also been included in Fig. 3c and d to show that both powders presented a homogeneous phase composition of Al and Ti, respectively.

The particle size distribution (PSD) of both powders (Fig. 3c) was practically monomodal and coarse-skewed, although the Al powder skewness was more significant. Regarding the quantitative results of the particle size measurements (inserted table in Fig. 3c), it can be highlighted that the 50 % of the particles population presented a particle diameter lower than 51.1 μm in the case of the Al powder, and lower than 24.8 μm for the Ti powder. Moreover, the distribution width of the Ti particles was larger, as reflected by the span of the distribution values: 1.54 and 2.94 μm for the Al and Ti particles, respectively.

The low spheroidicity of the employed particles does not represent a problem for CS deposition [41]. The CSAM deposition has the challenge of reducing the manufacturing costs, and using irregular water-atomized feedstock powders helps to the costs reduction since spherical powders, obtained by plasma-atomizing or gas-atomizing, are much more expensive than the same chemical composition water-atomized one [42]. For CS, the high kinetic energy imposed to the spraying particles results in a severe plastic deformation at the impact onto the substrate, suppressing the deleterious irregular shape effect on the porosity or bonding mechanisms.

The investigation of the particles' cross-sections indicated that the Al particles presented internal porosity, while the Ti particles did not show such porosity (Fig. 4a and b). The EDX analysis proved that the particles' chemical composition was pure Al and pure Ti, as indicated by EDX 1 and 2, respectively (Fig. 4c). The EDX results showed a peak for C content; however, this element refers to contamination, or to the adhesive tape used to hold the metallic particles for the analysis, and it is

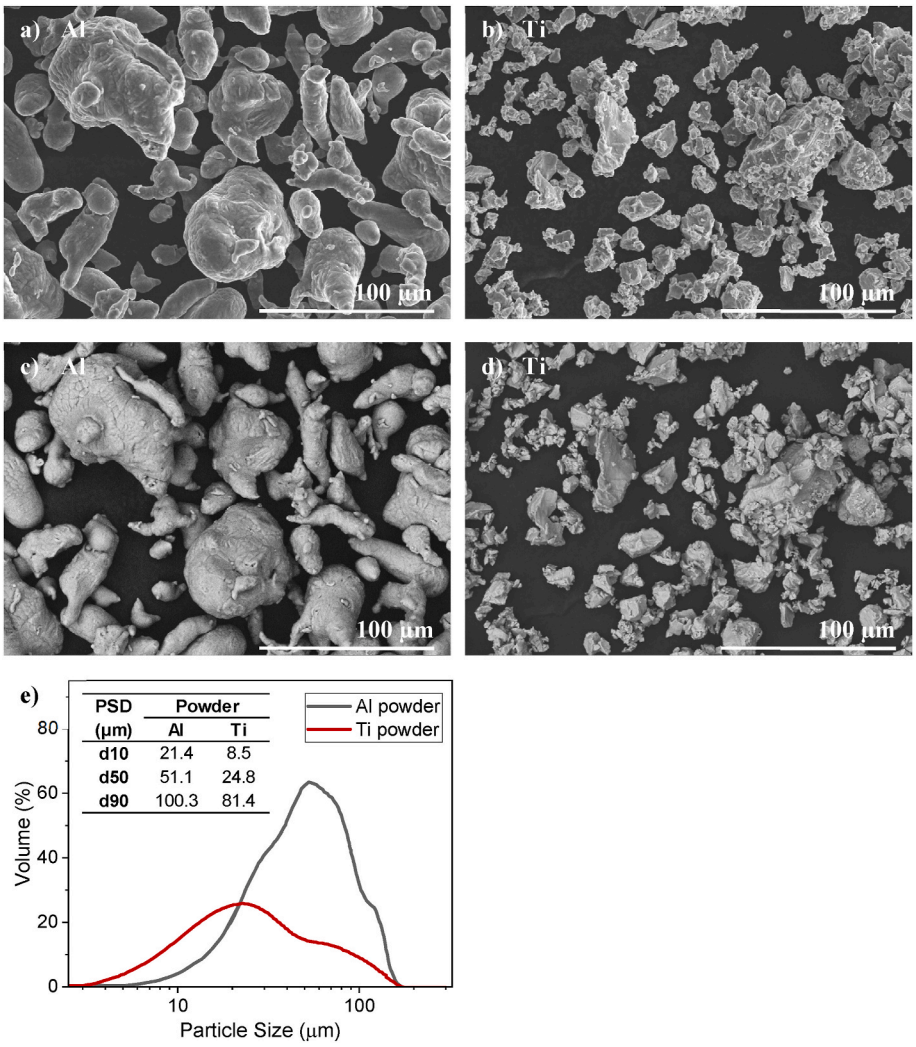

Fig. 3. SEM (SEI and BSE) micrographs of the Al (a and c) and Ti (b and d) feedstock powders. e) Particle size distribution in volume percentage of the feedstock powders with and inserted table indicating the d10, d50 and d90 parameters.

not related to the powders chemical composition. Moreover, a detailed analysis of the powders revealed that there was little contamination with iron oxide and steel particles in both feedstock powders. An example of this contamination is presented in the Al powder image in Fig. 4a, with the corresponding EDX in Fig. 4d. The presence of these particles was insignificant within the powder, as can be seen in Fig. 3c and d, where no signs of contamination was detected over a representative area of the powder.

3.2. Surface topography characterization of the CSAM samples

A first visual examination of the samples revealed that the different CS deposition strategies had led to different surface topographies, which were significantly characterized by the regular pattern generated by the spraying lines. Therefore, the samples' topography was analyzed as the sum of their surface form, waviness, and roughness. The waviness was associated with the periodic profile produced due to the different line spacings. Conversely, the roughness (shorter wavelengths) corresponded to the surface topography irregularities, and the form (highest wavelengths) was related to the surface macro-contour.

Fig. 5 presents representative examples of the profiles subtracted from the surface topography of all the samples, and the calculated roughness and waviness parameters are reported in Fig. 6. The graphs in Fig. 5 show that the waviness presented the predicted periodic profile. Moreover, it was observed that its wavelength and amplitude (peak to valley distance) were larger in the MK samples than in the T ones for the Al and Ti samples. The waviness wavelength in the MK samples was about 4 mm, while in the T samples was about 2 mm. Moreover, the marked differences in amplitude are reflected by the waviness parameters in Fig. 6a. It can be also observed that the values of the W_q parameter were similar to that of the W_a, indicating that the height irregularities were homogeneous. Besides that, the roughness was also higher in the MK samples (Fig. 6b), although there was no periodic pattern in this profile (Fig. 5). As the feedstock particle size was the same independently of the CS method, the roughness may be also a consequence of the strategy. Particularly, this fact could be associated to the porosity of the CS deposits, as it is discussed later.

Comparing the Al and the Ti deposits sprayed with the MK strategy, it was observed that the waviness presented a larger amplitude on the Al-MK samples than on the Ti-MK ones. The W_z parameter was 531 ± 70 µm for the Al-MK sample and 296 ± 85 µm for the Ti-MK sample (Fig. 6a), which means that there is a 44 % difference between them. These differences in the waviness profiles were not observed between the Al-T and Ti-T samples. Conversely, the roughness results were similar for both, the Al and Ti samples, comparing the same spraying strategy (Fig. 6b).

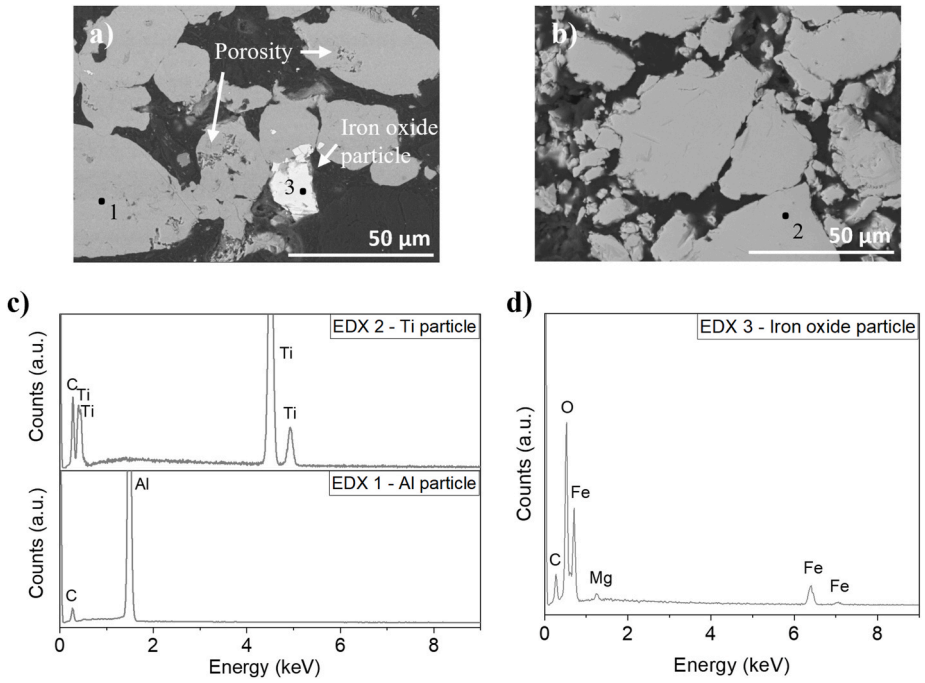

Fig. 4. SEM (BSEI) images of the feedstock a) Al and b) Ti particles' cross-sections; c) EDX analysis corresponding to an Al particle (points 1 in (a)) and to a Ti particle (point 2 in (b)); d) EDX analysis corresponding to an iron oxide particle (point 3 indicated in (a)).

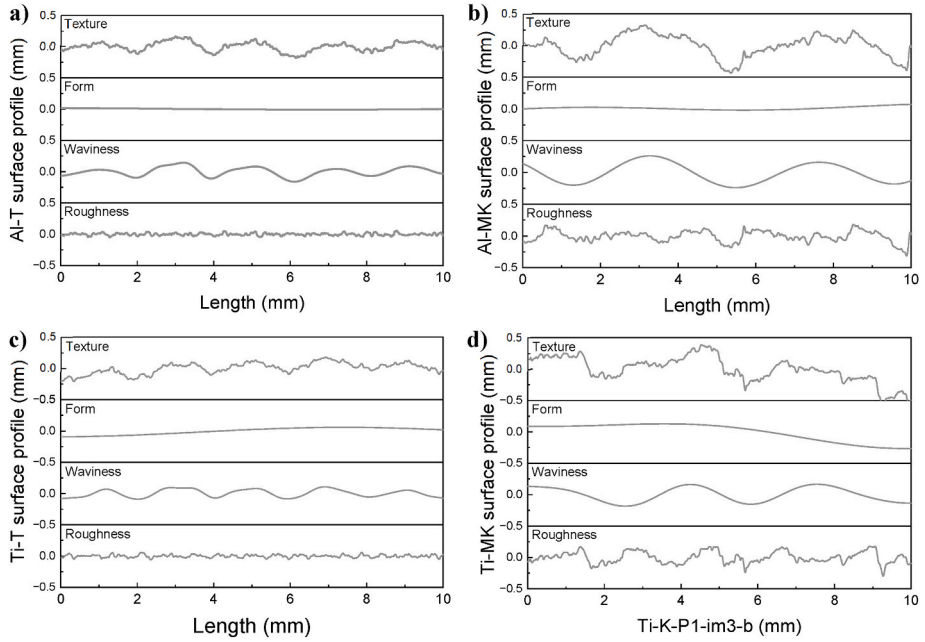

Fig. 5. Roughness, waviness, and form profiles extracted from the a) Al-T, b) Al-MK, c) Ti-T, and d) Ti-MK samples.

3.3. Microstructural characterization of the CSAM samples

Fig. 7 presents OM images of the samples' cross-sections, indicating their average thicknesses and porosities. The samples presented larger thicknesses than a typical sprayed coating, as these samples were sprayed to approach to an AM process. The thickness values were found between 4.7 and 9.6 mm (Fig. 7). Considering the different sample manufacturing methods, it was observed that the MK samples presented significantly higher thicknesses and average porosities as compared to the T ones. Besides that, comparing the different materials, the Ti samples were slightly denser and had a lower thickness than the Al ones.

The pores presented irregular shapes, and they were distributed in the interparticle region in all the samples (Fig. 7). Regarding their size, it was observed that the pore size distribution was more heterogeneous in the MK samples than in the T samples (Fig. 7). Moreover, the MK samples presented larger pores, showing a maximum length of about 500 µm, while the larger pore length in the T samples was about 100 µm. In addition, the porosity distribution along the MK samples' thicknesses was observed to be heterogeneous, as it is presented in Fig. 7b. This graph indicates that the MK samples presented a high porosity, especially at the top surface nearest area region (latest deformed particles in the spraying process). Conversely, the T samples showed a uniform

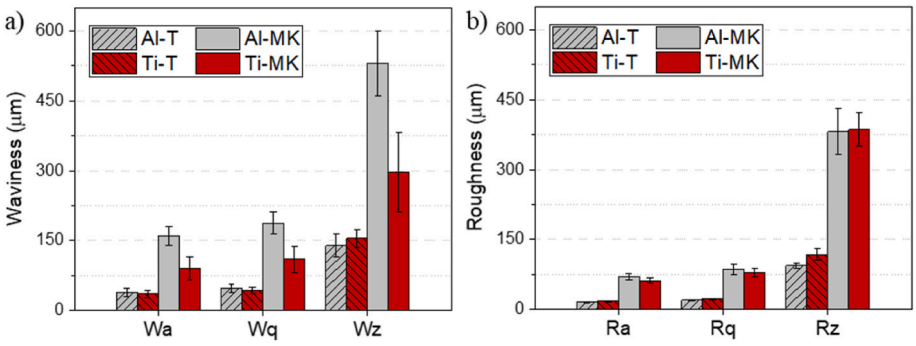

Fig. 6. a) Waviness and b) roughness parameters of the Al-T, Al-MK, Ti-T, and Ti-MK samples.

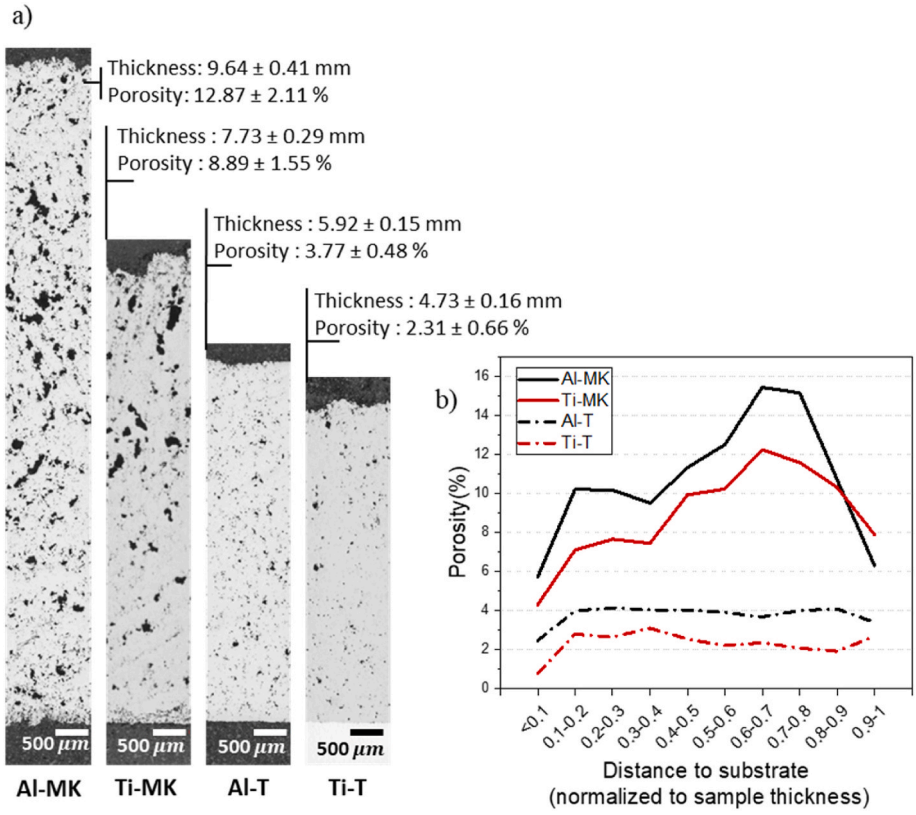

Fig. 7. a) OM images of the Al-T, Al-MK, Ti-T, and Ti-MK samples cross-sections showing the different porosity distributions and thicknesses. The average thickness and porosity values of each sample are indicated at the top of the corresponding sample. b) Porosity distribution along the samples' thicknesses of the Al-T, Al-MK, Ti-T, and Ti-MK. The distance from the interface with the substrate until the sample surface is normalized to the sample's thicknesses.

porosity distribution along the samples thickness.

Fig. 8 shows representative SEM images of the coatings cross section. Comparing these images with those shown in Fig. 4, relative to the powder, it can be observed that there is no change in the phases observed in the microstructure. This result agrees with the characteristics of the cold deposition technique. Since the spraying temperature is lower than the melting point of the material, the generation or change in microstructural phases is limited. Additionally, the SEM microstructural examination of the samples showed that the splats were adequately bonded to each other, despite the present porosity in the interparticle region, as can be observed in Fig. 8. Moreover, the chemical composition of the feedstock powder was proven to be maintained as Al and Ti correspondingly. The steel particles that were found in the initial feedstock powder were also observed dispersed along the samples, as the one indicated in Fig. 8b.

3.4. Mechanical properties characterization of the CSAM samples

Fig. 9a presents the H_0 values obtained along the samples' thicknesses, each value corresponds to the mean value of the H_0 measured from at least ten indents performed at a particular distance from the substrate. The distances at which the ten-indentation lines were performed are depicted in Fig. 9b, which corresponded to percentage distances as regard to the total sample thickness of 25 %, 50 %, and 75 %. This figure reveals that there was not a significant variation of hardness with the distance to the substrate location during deposition for any of the samples. The average H_0 values for each sample are reported in Table 4, along with the E measurements performed by nanoindentation. These results indicate no effect of the CS strategy on the samples' mechanical properties at the local scale. The T and MK strategies led to similar H_0 and E results for each material. Besides that, the obtained mechanical properties for the Al and Ti samples were in accordance with

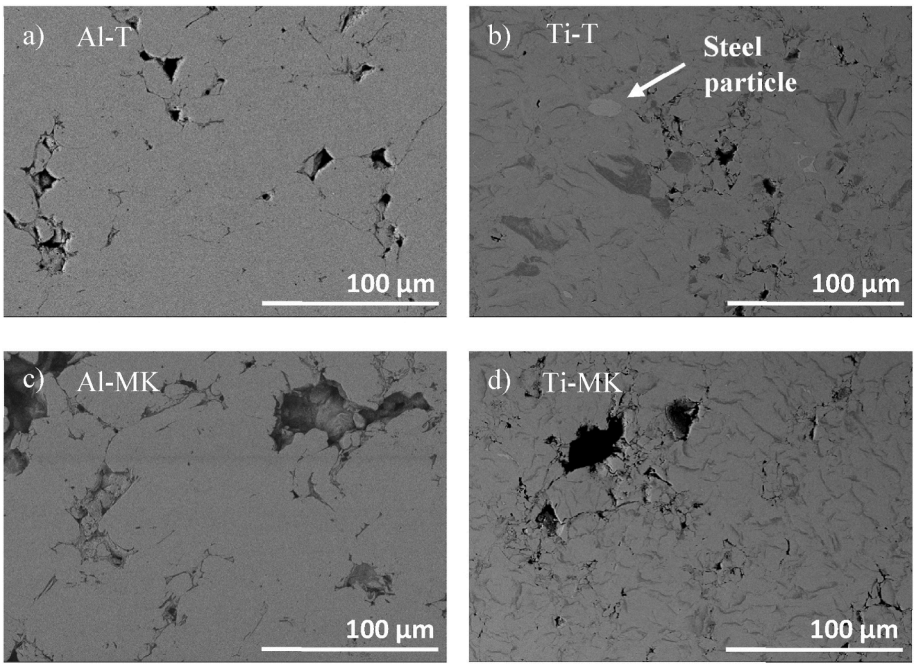

Fig. 8. SEM (BSEI) images showing the microstructure of the cross-sections of the a) Al-T, b) Ti-T, c) Al-MK, and Ti-MK samples.

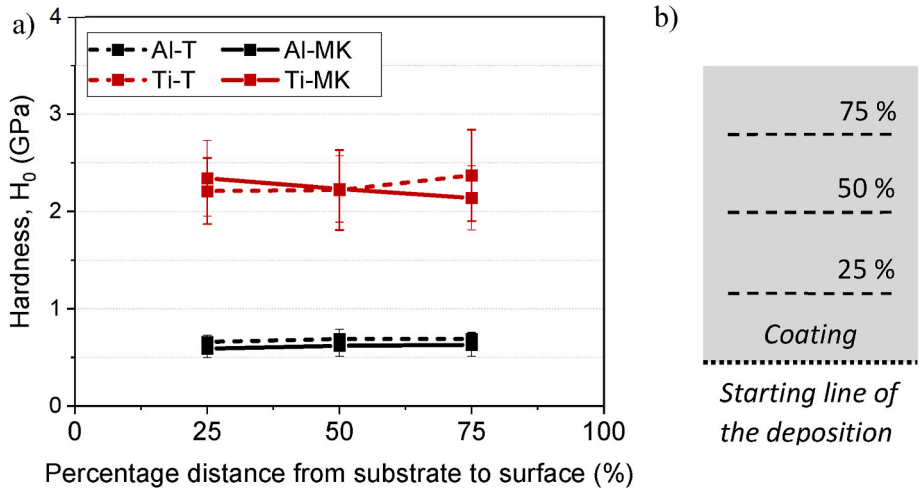

Fig. 9. a) H_0 average values at different distances from the substrate for the Al-T, Al-MK, Ti-T, and Ti-MK samples. b) Schematic representation of the three distances from the starting line of the deposition (substrate interface) at which the ten-indentation lines to measure the H_0 average values were performed. The distances correspond to the 25 %, 50 %, and 75 % length regarding to the total samples' thicknesses.

Table 4
H_0 and E measurements performed on the cross-sections of the Al-T, Al-MK, Ti-T, and Ti-MK samples. The H_0/E ratio is also included.

Material	H_0 (GPa)	E (GPa)	H_0/E
Al-T	0.68 ± 0.08	70.2 ± 3.0	$(9.7 \pm 1.2)\cdot10^{-3}$
Al-K	0.61 ± 0.10	72.2 ± 2.3	$(8.4 \pm 1.4)\cdot10^{-3}$
Ti-T	2.26 ± 0.41	99.0 ± 5.7	$(2.28 \pm 0.43)\cdot10^{-2}$
Ti-K	2.25 ± 0.36	99.8 ± 4.7	$(2.25 \pm 0.38)\cdot10^{-2}$

literature. The reported H_0 and E are 40–50 HV [43] and 69 GPa [44] for pure Al, and 235 HV and 102 GPa for pure Ti [45].

The H_0/E ratio was also calculated for each material, and it is included in Table 4. The H_0/E ratio is related to the deformation limit before permanent strain is caused [46]. Therefore, it can be related to the surface asperities resistance to plastically deform, and thus, to wear. The results showed that this ratio was higher in the Ti samples than in the Al samples. Conversely, the comparison of the H_0/E ratio between the T or MK strategies did not show significant differences.

4. Discussion

In this work, the CSAM technique has been again highlighted as a process that allows to manufacture components with a geometry near to the final shape. Therefore, the CSAM deposition has the ability of reducing the machining fabrication step, and thus its associated economic and environmental costs. Moreover, the final machining step can be further reduced if it is not necessary to rectify the surface of the as-sprayed sample. Therefore, the present study was designed to investigate the influence of the CS fabrication method on the surface topography of the as-sprayed samples.

Two different manufacturing strategies were used: following a T path

and the sequence known as MK. The results indicated that the different CSAM processes had certainly generated distinct surface topographies. The topography profile was a consequence of different spraying parameters: the angle of the spraying gun with the substrate, the step between spraying lines, the stand of distance and the radius of the circular movement described by the gun. Both strategies, T and MK, have generated a waviness profile with a characteristic periodic wavelength, which was controlled by the spacing step between spraying lines, regardless of the used material (Al or Ti). The step is the distance between the repeated movement described by the gun. In the T strategy, the gun movement consists of parallel lines with the gun normal to the substrate plane, and the MK consists of impressed circles with the gun in off-normal angles [6]. The used step in the T strategy was equal to 1 mm, while the wavelength was measured as 2 mm. Conversely, the MK strategy showed a waviness profile with a wavelength of 4 mm and the spraying step was of 2 mm. Besides that, the amplitude of the MK samples was at least two times that of the T ones (Fig. 6). These differences were also related to the distinct spraying parameters, as previous research in the field has pointed out that the waviness amplitude depends on the step distance, the gun velocity, the powder feed and the number of layers (the total thickness) [47,48].Conversely, the Al-MK samples were shown to present higher waviness amplitude than in the Ti-MK, showing a difference of a 44 % in W_a (Fig. 6). This observation was less marked in the T samples, with a W_a difference of a 9 %. Nevertheless, the differences between Al and Ti are not comparable, as they are related to the combination of the spraying parameters with the distinct particles' characteristics (size, morphology, mechanical properties, etc.).

The roughness profile was obtained after applying filters to remove the contributions with a wavelength larger than 2.5 mm and 0.8 mm for the MK and T samples, respectively. The MK samples also presented more pronounced amplitudes in the surface irregularities as compared to the T strategy irrespective of the material (Fig. 6). These amplitudes were in general lower than those of the waviness profile. However, the R_z parameter in the case of the Ti-MK sample was larger than that of the W_z. This outcome was associated to the higher porosity generated in the MK samples. Both parameters, roughness and porosity are generally related, as both of them depend on the particle accommodation ability [49]. The microstructural analysis indicated that the MK samples exhibited higher porosity percentages as compared to the T samples.

Comparing Figs. 4 and 8, no differences have been observed between the microstructure of the feedstock powders and that of the coatings. Besides that, the microstructural analysis has revealed that the MK strategy produced thicker samples, and with a higher level of porosity than the T samples. This observation was similar for the Al and Ti samples. Moreover, the Ti samples presented lower porosity as compared to the Al samples. This result was unexpected, because CSAM samples fabricated with ductile materials are usually denser than those sprayed with stiffer materials, as it has been proven by Vaz et al. [6] in their work on CSAM parts of 316L stainless steel, pure Cu, pure Al, pure Ti, and Ti6Al4V using MK and traditional strategies. However, the opposite trend observed in the present study was associated to the particle's morphology. The angular particle morphologies in Ti powder has been reported to produce lower porosity samples than spherical or sponge morphologies [50]. Conversely, it should be noted that the porosity is generally related to the particles velocity, which mainly depends on the spraying gas pressure and temperature [51]. The higher the particle velocity upon impact, the higher energy amount is spent on the plastic deformations of the particle, and thus, the particles enhance their accommodation capacity [51]. In addition, the porosity heterogeneity noticed in the MK samples was precisely explained to be a consequence of the different plastic deformation degrees to which each CS layer is subjected. The first deposited particle layers are subjected to subsequent plastic deformation caused by the following particles that are impacting on them [51]. Nevertheless, further research should consider the optimization of the coatings porosity by controlling the gas pressure and temperature. Besides that, the porosity level can be reduced by means of post-processing, such as thermal treatments [8,52]. Moreover, the EDX microanalysis investigation revealed that the chemical composition of the samples was similar to that of the feedstock powders.

The deposition strategy was shown to have a negligible effect on the mechanical properties of the samples, at the local scale (Table 4). The hardness was measured by nanoindentation, what allows the evaluation of this parameter regarding the material itself, without the influence of microstructural defects. The results showed that there was no effect of the deposition strategy on the E and H_0 values of the samples. The T and MK samples presented similar hardness values for both studied materials (Table 4). Moreover, the measured elastic moduli were in accordance with the bulk properties for Al and Ti, respectively, while the H_0 of the CS deposits was slightly increased. The reported E and H_0 for pure Al are 69 GPa and 20–45 HV (0.19–0.44 GPa) [53], and the obtained H_0 measured in the Al-T and Al-MK samples were 0.61–0.68 GPa. Conversely, the literature values of E and H_0 for pure Ti (Grade 2) are 103 GPa and 199 HV (1.45–1.95 GPa) [54,55], and the measured H_0 in the Ti-T and Ti-MK were 2.26–2.25 GPa. This increment in H_0 was explained by the work hardening induced during the CS deposition due to the plastic deformation experienced by the deposited particles [51].

Additionally, the H_0/E ratios of each studied material (Table 4) has shown that the deformation ability before permanent deformation was higher in the Ti samples than in the Al ones. Therefore, the wear resistance of the surface asperities is expected to be higher in Ti, with no significant differences between the T or MK deposition strategy.

In summary, the different CS strategies, T and MK, have been shown to influence the topography, thickness and porosity of the samples, while no effect on the mechanical properties was observed. Besides that, this outcome has been proved for both studied materials, pure Al and pure Ti. Therefore, it is apparent that the effect of the CS strategy on the coating's properties would be similar for all materials.

4.1. Modelling the topography profile though spectral analysis

The decomposition of the topography profile that has been conducted in section 3.2 proved that the original topography is a combination of different profiles (form, waviness, and roughness). Each profile has been isolated by applying frequency filters to the topography profile after discriminating the frequency ranges that corresponded to each profile. It should be noted that each individual profile can be constructed as a superposition of sinusoidal waves. The fast Fourier transform (FFT) of the original topography profile provides the amplitude-frequency spectrum, which reveals the more characteristic frequencies that constitute the original topography. Therefore, the most characteristic frequencies for each sub-profile can be identified by considering their corresponding frequency ranges. Then, the waves superposition can be done as expressed in equation (5), as a superposition of sinusoidal waves.

$$f(x) = \sum_{i=1}^{n} A_i \sin(2\pi f_i x + \varphi_i) \qquad \text{Equation 5}$$

Fig. 10 presents a representative example of the reconstructed profiles for the Al-MK sample. The most characteristic frequencies are pointed in the amplitude-frequency graph (Fig. 10a), as well as the frequency ranges that determine the form (ν_f), waviness (ν_w) or roughness (ν_r). The first peak in the amplitude-frequency spectrum (Fig. 10a) corresponds to a frequency of 0.090 mm^{-1}. The waviness principal peak was 0.270 mm^{-1}, which corresponds to a wavelength of 3.7 mm, similar to the measured RSm, 4 mm (Table 3). The selected main frequencies with their amplitudes were used to reconstruct the different profiles by means of the function defined in Equation (1), and these graphs are shown in Fig. 10b. Furthermore, it was observed that the original topography (without the form contribution) was similar to the calculated topography profile by means of the waves superposition, also

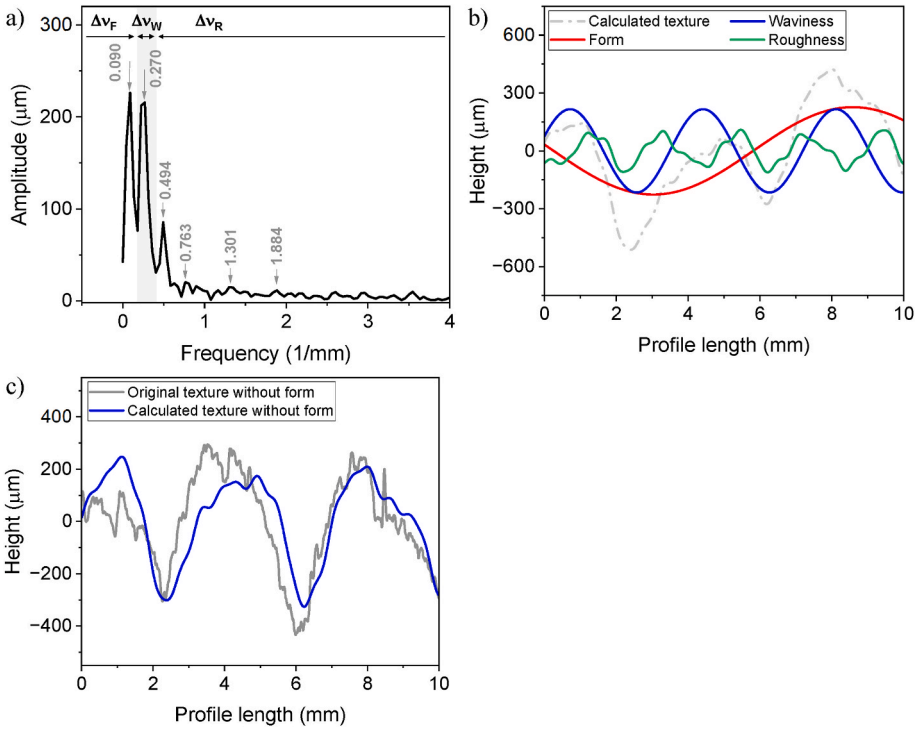

Fig. 10. a) Amplitude-frequency spectrum obtained by FFT corresponding to the original topography of the Al-MK sample; b) the texture, form, waviness and roughness constructed profiles for the same sample; and c) the original and calculated topography profiles without the form contribution to compare the similarity between both profiles.

without the form (Fig. 10c).

Table 5 reports the characteristic frequencies and associated amplitudes to construct a representative profile of each one of the studied samples in this paper. The frequencies corresponding to the form have not been added, as they are aleatory, they are not related to the spraying parameters or materials characteristics. To characterize the waviness, it is given only one frequency value due to the periodicity character of this profile. This frequency is related to the inverse RSm value of the T and MK samples, 2 and 4 mm respectively, as indicated in Table 3. The waviness frequency range was therefore selected as the frequency value equal to the inverse of the RSm value. Conversely, the roughness was characterized by means of several frequencies because this profile was not periodic. Regarding the amplitudes, the obtained values were similar to those obtained through the roughness analysis performed in section 3.2.

Therefore, this method allows to obtain a simplified profile of the surface topography of the samples. This simplified profile can be helpful to evaluate properties in which the topography is relevant, such as friction and wear, adhesion or wettability.

Consequently, this study has demonstrated the notable differences that can be created on the surface topography through the selection of the CSAM spraying parameters. In addition, studying the topography considering the generated pattern at different wavelengths provides a more complete and useful analysis for the material properties investigation, in which the surface topography plays a crucial role. The surface topography is known to be one of the multiple parameters that influence the wear response, which is one of the properties that are necessary to evaluate the typical final use of Ti and Al samples as structural materials. In this case, the contact between two bodies should be studied considering the real contact area, which is the contact of the surface asperities. Therefore, it is important to consider the irregularities size and distribution, which are described by the topographic analysis at different cut-off wavelengths. Besides that, the surface topography also has a crucial role in other properties such as hydrophobicity, adhesion, or optical properties.

Table 5
Characteristic frequencies (ν_{ch}) and associated amplitudes to construct a representative topography profile of the Al-T, Al-MK, Ti-T, and Ti-MK samples.

CS sample	ν_{ch} (1/mm)/Amplitude (µm)	
	Waviness profile	Roughness profile
Al-T	0.511/58	0.818/29
		1.328/8
		2.453/11
		3.168/7
Al-MK	0.270/216	0.494/85
		0.763/20
		1.301/15
		1.884/11
Ti-T	0.486/32	0.840/18
		1.371/9
		2.167/10
		3.007/7
Ti-MK	0.244/134	0.489/70
		1075/25
		1.270/30
		1.662/25

5. Conclusions

The effect of two different CSAM deposition methods on the surface topography was evaluated. The deposition strategies evaluated are particularly distinguished by the described CS gun trajectory, one following the traditional sequence (T) and the other based on an unconventional path (MK). The study was performed on two different materials, Al and Ti. This study's findings indicate that the as-sprayed samples surface topography is significantly influenced by the CSAM strategy. In addition, the effect of the deposition strategy was similar for both studied materials, Al and Ti. The MK strategy generated a topography with larger waviness and roughness wavelengths than those created with the T strategy. The waviness wavelength was related with

the spraying line spacing. Moreover, it has been shown that the topography investigation by analyzing the different wavelength ranges provide a more realistic description of the sample irregularities.

Regarding the microstructural properties, the MK strategy generated thicker samples and with a higher porosity than the T strategy for both, Al and Ti. Finally, the strategies evaluated, T and MK, did no effect on the mechanical properties, E and H_0, at the local scale. The H_0 of the samples was slightly increased as compared to the bulk materials, but that increment was similar regardless the used deposition strategy. Besides that, the H_0/E ratio indicated that the surface asperities of the Ti samples should present a higher wear resistance as compared to the Al samples.

This study highlights the potential of the different CSAM strategies to control the surface topography of the manufactured parts. Future research should consider the influence of these evaluated topography and properties on the performance of the samples regarding to abrasive wear, wettability, optical behavior, or any other property for which the topography is significant.

CRediT authorship contribution statement

Paloma Sirvent: Writing – original draft, Methodology, Investigation, Formal analysis, Conceptualization. **Ana Lozano:** Writing – original draft, Methodology, Investigation, Formal analysis, Conceptualization. **Miguel A. Garrido-Maneiro:** Writing – review & editing, Writing – original draft, Supervision, Methodology, Funding acquisition, Conceptualization. **Pedro Poza:** Writing – review & editing, Supervision, Methodology, Funding acquisition, Conceptualization. **Rordolpho F. Vaz:** Writing – review & editing, Methodology, Investigation, Conceptualization. **Vicente Albaladejo-Fuentes:** Methodology, Investigation, Conceptualization. **Irene G. Cano:** Supervision, Methodology, Funding acquisition, Conceptualization.

Declaration of competing interest

The authors declare that they have no known competing financial interests or personal relationships that could have appeared to influence the work reported in this paper.

Acknowledgements

The authors would like to acknowledge the financial support received from the Spanish government through the program MICIU/AEI /10.13039/501100011033 [grant numbers PID2020-115508RB-C21, PID2020-115508RB-C22 (A3M)]; and European Union – Next Generation EU through INVESTIGO program [grant number URJC-AI-19]. The author V. Albadalejo-Fuentes is a Serra Hunter Fellow.

References

[1] Gibson I, Rosen D, Stucker B, Khorasani M. Business and societal implications of AM. In: Gibson I, Rosen D, Stucker B, Khorasani M, editors. Addit. Manuf. Technol. Cham: Springer International Publishing; 2021. p. 649–61. https://doi.org/10.1007/978-3-030-56127-7_22.

[2] Yin S, Aldwell B, Lupoi R. Cold spray additive manufacture and component restoration. In: Cavaliere P, editor. Cold-spray coatings recent trends futur. Cham: Springer; 2018. p. 195–224. https://doi.org/10.1007/978-3-319-67183-3_6.

[3] Pathak S, Saha GC. Development of sustainable cold spray coatings and 3D additive manufacturing components for repair/manufacturing applications: a critical review. Coatings 2017;7. https://doi.org/10.3390/coatings7080122.

[4] Assadi H, Schmidt T, Richter H, Kliemann JO, Binder K, Gärtner F, Klassen T, Kreye H. On parameter selection in cold spraying. J Therm Spray Technol 2011;20:1161–76. https://doi.org/10.1007/s11666-011-9662-9.

[5] Poza P, Garrido-Maneiro MÁ. Cold-sprayed coatings: microstructure, mechanical properties, and wear behaviour. Prog Mater Sci 2022;123. https://doi.org/10.1016/j.pmatsci.2021.100839.

[6] Vaz RF, Albaladejo-Fuentes V, Sanchez J, Ocaña U, Corral ZG, Canales H, Cano IG. Metal knitting: a new strategy for cold gas spray additive manufacturing. Materials 2022;15:1–17. https://doi.org/10.3390/ma15196785.

[7] Wu H, Xie X, Liu M, Verdy C, Zhang Y, Liao H, Deng S. Stable layer-building strategy to enhance cold-spray-based additive manufacturing. Addit Manuf 2020;35:101356. https://doi.org/10.1016/j.addma.2020.101356.

[8] Garfias A, Vaz R, Albaladejo-Fuentes V, Sánchez J, Cano IG. Geometry and microstructure control of remanufactured metallic parts by cold spray additive manufacturing. Materials 2023;16. https://doi.org/10.3390/ma16134735.

[9] Kucharski S, Starzynski G. Study of contact of rough surfaces: modeling and experiment. Wear 2014;311:167–79. https://doi.org/10.1016/j.wear.2014.01.009.

[10] Grützmacher PG, Rosenkranz A, Szurdak A, Grüber M, Gachot C, Hirt G, Mücklich F. Multi-scale surface patterning – an approach to control friction and lubricant migration in lubricated systems. Ind Lubric Tribol 2019;71:1007–16. https://doi.org/10.1108/ILT-07-2018-0273.

[11] Wu S, Zhang B, Liu Y, Suo X, Li H. Influence of surface topography on bacterial adhesion: a review (Review). Biointerphases 2018;13(6):060801. https://doi.org/10.1116/1.5054057.

[12] Guo C, Wang XW, Yuan ZH. Pore diameter-dependence wettability of porous anodized aluminum oxide membranes. J Porous Mater 2013;20:673–7. https://doi.org/10.1007/s10934-012-9641-7.

[13] Costa HL, Schille J, Rosenkranz A. Tailored surface textures to increase friction—a review. Friction 2022;10:1285–304. https://doi.org/10.1007/s40544-021-0589-y.

[14] Wang B, Zhang W, Liu Z. Study of the impact of surface topography on wear resistance. Coatings 2024;14:1128. https://doi.org/10.3390/coatings14091128.

[15] Grabon WA, Grochalski K, Da Costa AR, Epasto G. New paradigm in surface topography transition vs. machining and wear process. Tribol Int 2024;191:109124. https://doi.org/10.1016/j.triboint.2023.109124.

[16] Sakhamuri MSD, Harvey TJ, Vierneusel B, Wood RJK. Wear induced changes in surface topography during running-in of rolling-sliding contacts. Wear 2023;522:204685. https://doi.org/10.1016/j.wear.2023.204685.

[17] Stachowiak GW, Batchelor AW. Fundamentals of contact between solids. In: Engineering Tribology, fourth ed. Boston: Butterworth-Heinemann; 2014. p. 475–524. https://doi.org/10.1016/B978-0-12-397047-3.00010-2.

[18] Rodríguez J, Poza P, Garrido MA, Rico A. Dry sliding wear behaviour of aluminium-lithium alloys reinforced with SiC particles. Wear 2007;262:292–300. https://doi.org/10.1016/j.wear.2006.05.006.

[19] Larsson R. Modelling the effect of surface roughness on lubrication in all regimes. Tribol Int 2009;42:512–6. https://doi.org/10.1016/j.triboint.2008.07.007.

[20] Leese H, Bhurtun V, Lee KP, Mattia D. Wetting behaviour of hydrophilic and hydrophobic nanostructured porous anodic alumina. Colloids Surfaces A Physicochem. Eng. Asp. 2013;420:53–8. https://doi.org/10.1016/j.colsurfa.2012.12.010.

[21] Goyal T, Walia RS, Sidhu TS. Surface roughness optimization of cold-sprayed coatings using Taguchi method. Int J Adv Manuf Technol 2012;60:611–23. https://doi.org/10.1007/s00170-011-3642-6.

[22] Shao L, Xue N, Li W, Liu S, Tu Z, Chen Y, Zhang J, Dai S, Liu Q, Shi X, Wang T, Chen M, Huang Y, Xu F, Zhu L. Effect of cold-spray parameters on surface roughness, thickness and adhesion of copper-based composite coating on aluminum alloy 6061 T6 substrate. Processes 2023;11. https://doi.org/10.3390/pr11030959.

[23] Gadelmawla ES, Koura MM, Maksoud TMA, Elewa IM, Soliman HH. Roughness parameters. J Mater Process Technol 2002;123:133–45. https://doi.org/10.1016/S0924-0136(02)00060-2.

[24] Seabra J, Berthe D. Influence of surface waviness and roughness on the normal pressure distribution in the hertzian contact. J Tribol 1987;109:462–9. https://doi.org/10.1115/1.3261472.

[25] Tomanik E, El Mansori M, Souza R, Profito F. Effect of waviness and roughness on cylinder liner friction. Tribol Int 2018;120:547–55. https://doi.org/10.1016/j.triboint.2018.01.012.

[26] Li Y, Garabedian N, Schneider J, Greiner C. Waviness affects friction and abrasive wear. Tribol Lett 2023;71:1–12. https://doi.org/10.1007/s11249-023-01736-1.

[27] Venturi F, Gilfillan N, Hussain T. A convolution-based approach to cold spray additive manufacturing. Addit. Manuf. Lett. 2021;1:100014. https://doi.org/10.1016/j.addlet.2021.100014.

[28] Huang CJ, Chen T, Fu BL, Zhang ZM, List A, Wiehler L, Klusemann B, Li WY, Gärtner F, Klassen T. Ductility and fracture behavior of cold spray additive manufactured zinc. Addit Manuf 2024;89. https://doi.org/10.1016/j.addma.2024.104310.

[29] Vilardell AM, Cinca N, Garcia-Giralt N, Dosta S, Cano IG, Nogués X, Guilemany JM. Osteoblastic cell response on high-rough titanium coatings by cold spray. J Mater Sci Mater Med 2018;29:1–10. https://doi.org/10.1007/s10856-018-6026-8.

[30] Shah R, Pai N, Rosenkranz A, Shirvani K, Marian M. Tribological behavior of additively manufactured metal components. J. Manuf. Mater. Process. 2022;6. https://doi.org/10.3390/jmmp6060138.

[31] Veiga C, Davim JP, Loureiro AJR. Properties and applications of titanium alloys: a brief review. Rev Adv Mater Sci 2012;32:14–34.

[32] Rambabu RJH, P, Eswara Prasad, Kutumbarao N, Wanhill VV. Aluminium alloys for aerospace applications. In: Prasad R, Wanhill N, editors. Aerosp. mater. Mater. Technol. Singapore: Indian Institute of Metals Series. Springer; 2017. https://doi.org/10.1007/978-981-10-2134-3.

[33] ISO 4287:1997, Geometrical product specification (GPS) – surface texture: profile method – terms, definitions and surface texture parameters, n.d.

[34] ISO 4288:1998, Geometrical product specifications (GPS) - surface texture: profile method - rules and procedures for the assessment of surface texture, n.d.

[35] ISO 11562:1996, Geometrical Product Specifications (GPS) — surface texture: profile method — metrological characteristics of phase correct filters, n.d.

[36] ISO 21920:2023, GeOmetrical product specifications (GPS) - surface texture: profile - Part 1: indication of surface texture, n.d.
[37] Oliver WC, Pharr GM. An improved technique for determining hardness and elastic modulus using load and displacement sensing indentation experiments. J Mater Res 1992;7:1564–83. https://doi.org/10.1557/JMR.1992.1564.
[38] Gong J, Wu J, Guan Z. Examination of the indentation size effect in low-load vickers hardness testing of ceramics. J Eur Ceram Soc 1999;19:2625–31. https://doi.org/10.1016/S0955-2219(99)00043-6.
[39] Nix WD, Gao H. Indentation size effects in crystalline materials: a law for strain gradient plasticity. J Mech Phys Solid 1998;46:411–25. https://doi.org/10.1016/S0022-5096(97)00086-0.
[40] Oliver WC, Pharr GM. Measurement of hardness and elastic modulus by instrumented indentation: advances in understanding and refinements to methodology. J Mater Res 2004;19:3–20. https://doi.org/10.1557/jmr.2004.19.1.3.
[41] Vaz RF, Silvello A, Sanchez J, Albaladejo V, García-Cano I. The influence of the powder characteristics on 316l stainless steel coatings sprayed by cold gas spray. Coatings 2021;11:1–18. https://doi.org/10.3390/coatings11020168.
[42] Jandaghi MR, Pouraliakbar H, Iannucci L, Fallah V, Pavese M. Comparative assessment of gas and water atomized powders for additive manufacturing of 316 L stainless steel: microstructure, mechanical properties, and corrosion resistance. Mater Char 2023;204:113204. https://doi.org/10.1016/j.matchar.2023.113204.
[43] Abbasi M, Sajjadi SA. Determination of optimum condition for producing Al/Ni3Al composite powder using blending and mechanical milling. 9th Semin. Exp. Tech. Des. Compos. Mater. 2009:3–5.
[44] Lasagni F, Degischer HP. Enhanced Young's modulus of Al-Si alloys and reinforced matrices by co-continuous structures. J Compos Mater 2010;44:739–55. https://doi.org/10.1177/0021998309347649.
[45] Szpunar M, Trzepieciński T, Ostrowski R, Zwolak M. Research on forming parameters optimization of incremental sheet forming process for commercially pure titanium grade 2 sheets. Arch Metall Mater 2022;67:1411–8. https://doi.org/10.24425/amm.2022.141068.
[46] Ceballos L, Garrido MA, Fuentes V, Rodríguez J. Mechanical characterization of resin cements used for luting fiber posts by nanoindentation. Dent Mater 2007;23:100–5. https://doi.org/10.1016/j.dental.2005.12.007.
[47] Winnicki M, Małachowska A, Ambroziak A. Taguchi optimization of the thickness of a coating deposited by LPCS. Arch Civ Mech Eng 2014;14:561–8. https://doi.org/10.1016/j.acme.2014.04.006.
[48] Winnicki M, Małachowska A, Piwowarczyk T, Rutkowska-Gorczyca M, Ambroziak A. The bond strength of Al + Al2O3 cermet coatings deposited by low-pressure cold spraying. Arch Civ Mech Eng 2016;16:743–52. https://doi.org/10.1016/j.acme.2016.04.014.
[49] Lima RS, Kucuk A, Berndt CC, Karthikeyan J, Kay CM, Lindemann J. Deposition efficiency, mechanical properties and coating roughness in cold-sprayed titanium. J Mater Sci Lett 2002;21:1687–9. https://doi.org/10.1023/A:1020833011448.
[50] Wong W, Vo P, Irissou E, Ryabinin AN, Legoux JG, Yue S. Effect of particle morphology and size distribution on cold-sprayed pure titanium coatings. J Therm Spray Technol 2013;22:1140–53. https://doi.org/10.1007/s11666-013-9951-6.
[51] Villafuerte J, editor. Modern cold spray: materials, process, and applications. first ed. Springer; 2015. https://doi.org/10.1007/978-3-319-16772-5.
[52] Vaz RF, Garfias A, Albaladejo V, Sanchez J, Cano IG. A review of advances in cold spray additive manufacturing. Coatings 2023;13. https://doi.org/10.3390/coatings13020267.
[53] Spec. Mater. In: Committee ASMH, editor. Properties of wrought aluminum and aluminum alloys, prop. Sel. Nonferrous alloy, vol. 2; 1990. https://doi.org/10.31399/asm.hb.v02.a0001060. 0.
[54] Cossú CMFA, Vicente ED, Cardoso IGR, Schettini YS, De Ataíde Garcia Precioso J, Nunes CA, De Almeida LH, Borborema S. Mechanical and microstructural characterization of AS-CAST Ti-12Mo-xNb alloys for orthopedic application. Mater Res 2019;22:1–5. https://doi.org/10.1590/1980-5373-MR-2019-0178.
[55] Lim HS, Hwang MJ, Jeong HN, Lee WY, Song HJ, Park YJ. Evaluation of surface mechanical properties and grindability of binary Ti alloys containing 5 wt % Al, Cr, Sn, and V. Metals 2017;7:1–11. https://doi.org/10.3390/met7110487.